Rashba effects in lead-free ferroelectric semiconductor [CH$_3$PH$_3$]SnBr$_3$

Ravi Kashikar,[1,*] P. S. Ghosh,[1,2] S. Lisenkov,[1] A. Stroppa,[3,†] and I. Ponomareva[1,‡]

[1]*Department of Physics, University of South Florida, Tampa, Florida 33620, USA*

[2]*Glass & Advanced Materials Division, Bhabha Atomic Research Centre, Mumbai 400 085, India*

[3]*Consiglio Nazionale delle Ricerche, Institute for Superconducting and Innovative Materials and Devices (CNR-SPIN),*
c/o Department of Physical and Chemical Sciences, University of L'Aquila, Via Vetoio I-67100 Coppito, L'Aquila, Italy

First-principles density functional theory computations are used to predict Rashba effects cofunctional with ferroelectricity in a recently synthesized lead-free hybrid organic-inorganic perovskite MPSnBr$_3$ (MP=methylphosphonium, [CH$_3$PH$_3$]$^+$). The ground state of the material is polar monoclinic with calculated spontaneous polarization of 3.01 μC/cm^2. It exhibits near band edges' spin splitting of up to 3.3 meV and Rashba coefficient up to 0.62 eV Å. The spin textures have different topology in the conduction and valence band, which originates from the difference in the spin-momentum coupling strengths. They occur in two orthogonal planes of the Brillouin zone and are coupled to the direction of spontaneous polarization. These features persist at a finite temperature of 293 K. At 333 K, that is, above monoclinic to orthorhombic phase transition, spontaneous polarization is reduced to 0.15 μC/cm^2, while the maximum spin splitting and Rashba coefficient reduce slightly to the values of 2.9 meV and 0.41 eV Å, respectively. The spin textures remain coupled with the polarization direction. We investigate the dependence of the aforementioned properties on the choice of computational methodology to extend the first-principles predictions to include finite temperature effects. We find that the predictions are sensitive to the methodology. Our study reveals the potential of MPSnBr$_3$ for low-temperature applications in spintronics and quantum computing.

I. INTRODUCTION

Hybrid organic-inorganic perovskites (HOIP) are currently the focus of attention, owing to their outstanding chemical diversity and range of properties. They share the chemical formula, ABX_3, with inorganic perovskites but feature organic cation on the A site and, in some cases, organic ligands on the X site. Hundreds of HOIP have been synthesized up to date with properties ranging from optoelectronic to ferroelectricity [1–4]. They typically exhibit phase transitions, sometimes several, which often are of order-disorder type. In particular, high-temperature high symmetry phase is associated with the disorder of the A-site cation, while the temperature lowering results in ordering on the A site, which drives symmetry lowering. Perhaps the most celebrated example of HOIP is MAPbI$_3$ (MA is CH$_3$NH$_3$), which exhibits two phase transitions: from cubic to tetragonal at 330 K and from tetragonal to orthorhombic at 160 K. MAPbI$_3$ is also an example of halide HOIP [5]. Many HOIPs are semiconductors and some exhibit ferroelectric phases, although the typical polarization is below 5 μC/cm^2 [2,4], which is much smaller compared to the prototypical oxide perovskite ferroelectrics. Interestingly, some of such ferroelectric HOIPs have also been reported to possess Rashba-Dresselhaus spin splitting [6–10], which originates from spin-orbit coupling (SOC) [11,12]. Sizable

Rashba effect has been predicted in β-MAPbI$_3$, β-MASnI$_3$, and ortho-MASnBr$_3$, where MA is methylammonium [13], although a combined computational and experimental work ruled out the presence of a large static Rashba effect in bulk MAPbI$_3$ [14]. Twelve organohalide perovskites (A = MA, FA; B = Pb, Sn; X = Cl, Br, I) have been investigated computationally to predict fairly large Rashba (up to 200 meV) spin splitting [8].

Spin splitting leads to spin-momentum locking, which manifests in the existence of spin polarizations in momentum space or spin textures. Such spin-momentum locking is highly desirable for spin-charge interconversion and could find applications in spintronics and quantum computing [15–17]. In ferroelectrics, spin textures could couple to the electric polarization, which is known as ferroelectricity Rashba effects cofunctionality [18]. Such coexistence allows for the control of spin-momentum locking by the external electric field, which is highly desirable for practical applications [15]. The cofunctionality has been demonstrated in inorganic materials [18–20] and in some of the HOIPs [6,7,21,22]. For example, the possibility to control spin splitting by an applied electric field has been predicted in low-dimensional nanostructures made of CH$_3$NH$_3$PbX_3 (X = I, Br) [6]. Rashba-like band splitting, persistent spin texture, and/or spiral spin texture, which can be manipulated by tuning the ferroelectric or by the antiferromagnetic order parameter, were predicted from first-principles calculations in ferroelectric TMCM-MnCl$_3$ [TMCM = (CH$_3$)$_3$NCH$_2$Cl$^+$, trimethylchloromethyl ammonium] [21]. A followup study on the nonmagnetic counterpart TMCM-CdCl$_3$ predicted

*ravik@usf.edu

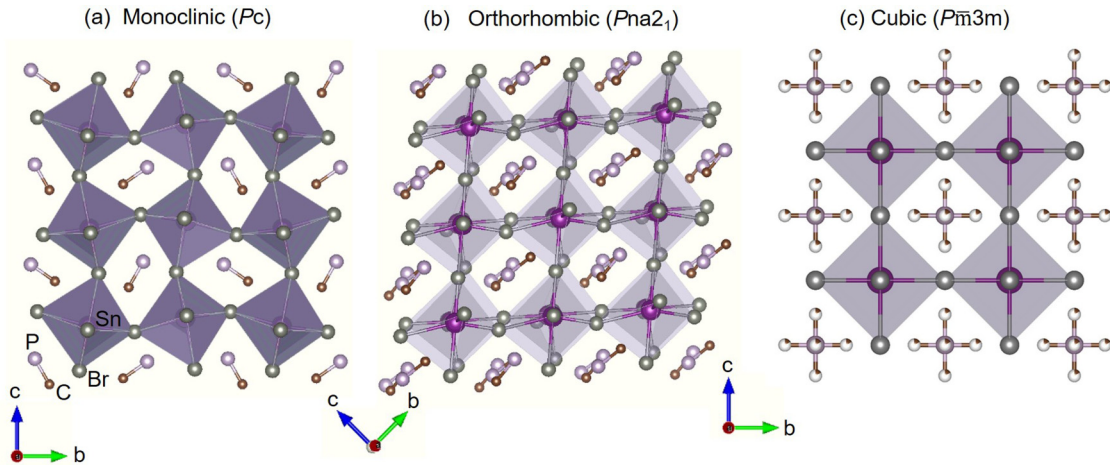†alessandro.stroppa@aquila.infn.it

‡iponomar@usf.edu

FIG. 1. Crystal structures of different phases of MPSnBr$_3$, without hydrogen atoms.

that spin textures in this family of materials are electrically and chemically tunable with significant enhancement of spin splitting possible through substitution of Cl with Br [22].

Recently, a three-dimensional lead-free MPSnBr$_3$ (MP is methyl phosphonium, [CH$_3$PH$_3$]$^+$) with a direct band gap of 2.62 eV has been synthesized and predicted to exhibit the above-room-temperature ferroelectricity [23]. It crystallizes in nonpolar cubic $Pm\bar{3}m$ phase at high temperature and undergoes a phase transition to polar orthorhombic $Pna2_1$ phase at 357 K, followed by a transition to polar monoclinic phase Pc at 314 K. These phases are shown in Fig. 1. The cubic phase is associated with the dynamical disorder of the MP molecule, while the orthorhombic and monoclinic phases are ordered. It was suggested to be a multiaxial ferroelectric with 6 and 12 polar axes in orthorhombic and monoclinic phases, respectively [23]. The latter number exceeds the one in other halide perovskites and even the classical inorganic perovskites. Moreover, group theoretical analysis predicts both polar phases to be (fully) ferroelectric and (partially) ferroelastic [24], which could open ways for both electrical and mechanical control of the electronic structure. Having these many desirable features, MPSnBr$_3$ may be a promising candidate for electrically tunable spin-charge interconversion. However, presently its potential for exhibiting Rashba effects and ferroelectric simultaneousness has not been revealed. Does the material exhibit sizable spin splitting and, if yes, how does it compare with other HOIP as well as the inorganic counterparts? Are the Rashba effects and ferroelectric cofunctionality affected by the temperature? How do these features change across phase transition between two experimentally reported polar phases?

The aims of this work are (i) to predict that lead-free HOIP MPSnBr$_3$ exhibits spontaneous polarization, near band edge spin splitting, and a variety of spin textures in both of its polar phases, (ii) to predict that in both phases, spin textures are coupled to the direction of polarization, that is the material exhibits ferroelectric and Rashba cofunctionality, (iii) to predict that these properties exist in a wide temperature range and report the associated temperature evolution, and (iv) to discuss methodological challenges of extending density

functional theory (DFT) predictions of the aforementioned properties to finite temperatures.

II. COMPUTATIONAL METHODOLOGY

DFT calculations have been carried out using the Vienna Ab initio Simulation Package (VASP) with Perdew-Burke-Ernzerhof (PBE) exchange-correlation functional and projector-augmented-wave (PAW) pseudopotentials [25,26]. To describe dispersive interactions, zero damping D3 dispersion corrections as proposed by Grimme *et al.* [27] were incorporated in the simulations. The plane wave basis was truncated at the energy cutoff of 600 eV. For integration inside the Brillouin zone we used $4 \times 6 \times 6$ and $6 \times 4 \times 4$ k-point meshes for monoclinic and orthorhombic phases, respectively. All structural relaxations are carried out using a conjugate gradient algorithm until ionic forces are less than 2 meV/Å and residual stresses are less than 0.05 GPa. All the electronic structure calculations are carried out with SOC.

The polarization is computed using the modern theory of polarization developed by King-Smith and Vanderbilt [28]. To avoid ambiguity due to polarization quantum, we constructed a rotodistortion path as proposed in Ref. [29] for experimentally reported monoclinic and orthorhombic phases and computed polarization along the path. The polarization along the path for a single polarization branch is given in Fig. 2. Along the path, the first and last points represent the experimental structure and its inversion, respectively. The spontaneous polarization is evaluated as half the difference between the values at the end points. This approach is inspired by the experimental route to polarization measurement which involves polarization reversal. We note that the polarization at the intermediate steps along the path depends on the choice of the rigid rotations for the molecules and is not unique. The purpose of these calculations is to make sure that the polarization of the end points is computed for the same polarization branch. The computational resolution for polarization calculations is 10^{-4} μC/cm^2. Once the polarization of the experimental structures is determined, we use it as a reference point for other structures. For example, to determine the polarization of a fully relaxed structure in the Pc space group,
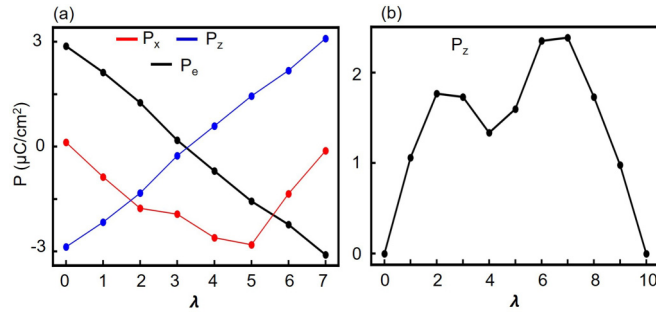
FIG. 2. Polarization components along the rotodistortion path for the experimental monoclinic (a) and orthorhombic (b) phases. For the monoclinic phase, we plot the projection onto the polar axis P_e to better illustrate reversal.

we connect it to the experimental Pc structure using ISOTROPY software [30,31] and compute the polarization along the path. The Cartesian axes x, y, and z are along **a**, **b**, **a** $\times$ **b** lattice vectors, respectively. We have computed the energy along the rotodistortion path in the monoclinic phase, which revealed the energy barrier of 0.074 eV/atom. Note that this value has not been optimized and therefore is the upper estimate of the barrier associated with homogeneous polarization reversal. Nevertheless, it is already within the surmountable limit of 1 eV/atom proposed in Ref. [18]. We followed Ref. [32] to compute the coercive field associated with such hypothetical homogeneous polarization reversal and obtained the value of 11.4 GV/m at room temperature. Residual depolarizing field is also known to decrease coercive field significantly [33]. Allowing for residual depolarizing field [32], taken here to be half of the one associated with ideal open circuit boundary conditions for a planar capacitor, reduces the coercive field down to 2.1 GV/m. This is, of course, the upper estimate for the coercive field as it assumes a hypothetical homogeneous polarization reversal and does not account for domain formations and propagation known to significantly lower co-

ercive fields [34]. Nevertheless, the coercive field in HOIP could be indeed quite large [23,32]. Therefore, we can classify MPSnBr$_3$ as ferroelectric. The barrier between the structure and its inversion in the monoclinic phase is 0.06 eV/atom, which may also be surmountable.

For finite temperature studies, we utilized *ab initio* molecular dynamics (AIMD), which is based on the Born-Oppenheimer approximation. The typical run was 10 ps long with a MD integration step of 0.5 fs. The temperature control was achieved with a Nose-Hoover thermostat as implemented in VASP. To decrease the computational cost, we use experimental lattice vectors and run NVT simulations rather than NPT simulations, which take longer to equilibrate. The time evolution of potential energy at 293 and 333 K is given in Fig. 3, which demonstrates that equilibrium is reached within 1 ps. The last 9 ps of simulations correspond to equilibrium and can be used for computing averages. Inspection of atomic trajectories and associated distribution functions revealed that during the indicated time, all but hydrogen atoms oscillate near their equilibrium positions. Figures 3(b), 3(c) and 3(e), 3(f) show some representative distribution functions for Sn and Br atomic positions from 293 and 333 K AIMD run, respectively. The distribution functions are narrow, with the average value (shown by a vertical line) close to the distribution peak. Therefore, average positions provide a reliable estimate for the ensemble average. Hydrogen atoms, however, perform the larger-scale motion. Thus the averaging is not meaningful. Therefore, we perform averaging for all but hydrogen atoms, then subject hydrogen atoms to ionic relaxation while keeping the rest of the ions at their ensemble-average position.

There exist other computational strategies to extend DFT predictions to finite temperatures [35–38]. For example, in Ref. [35] the effect of temperature on band structure was established through incorporation of electron-phonon coupling and thermal expansion. A similar strategy has been used in Refs. [36,37]. Etienne *et al.* quantified Rashba effect magnitude in MAPbI$_3$ under thermal conditions by simulating
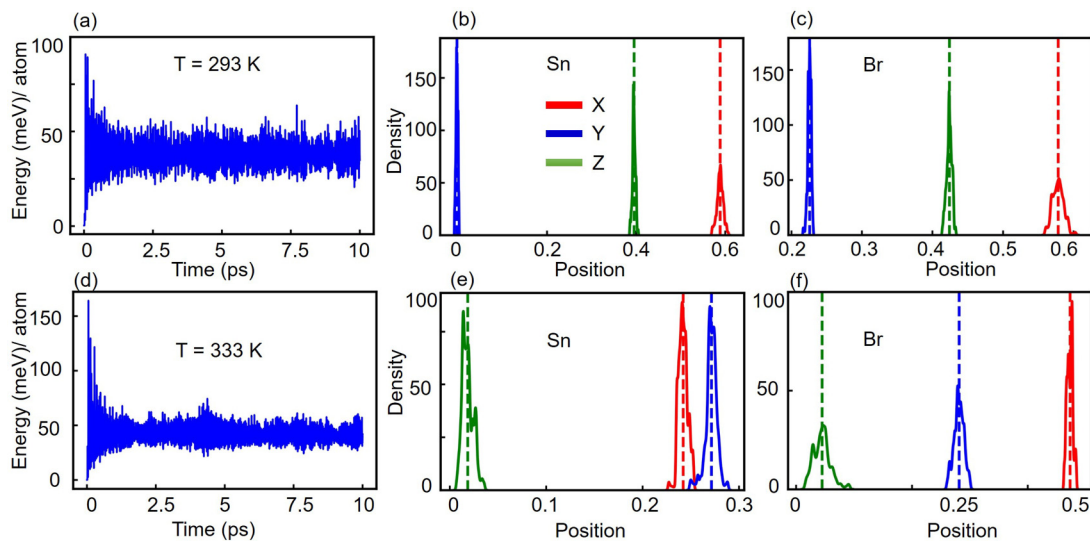

FIG. 3. Potential energy as a function of the AIMD step at 293 K (a) and 333 K (d). The energy is relative to the ground state. Distribution of positions for Sn and Br atoms in AIMD simulation at 293 K (b),(c) and 333 K (e),(f). Vertical lines give the average positions.

the material in AIMD and computing band structures on the subset of snapshots [38]. Sometimes, to extend predictions to high-temperature phases, structural relaxations of those phases are used and the properties are calculated for the relaxed structures [19,21,39]. In Ref. [14] it was argued that probing the potential energy surface at zero temperature, as is done in DFT structural relaxations, is inadequate to compute the structures of high-temperature phases and may result in erroneous predictions. Since the majority of Rashba effects and ferroelectricity is revealed from DFT computations [7,8,19,40] it is imperative to find out how the choice of computational methodology to investigate temperature effects may influence Rashba splittings and spontaneous polarization. To answer this question, we carry out simulations using five computational strategies for structure determination. The first one is to compute all properties for the experimental structure. Such strategy has been used to predict temperature dependence of band structure and Rashba parameter in Bz_2PbCl_4 [6]. We label associated structures as Expt. In principle, in this case, one could expect to obtain properties which match experimental findings most closely. At the same time in some cases experimental resolution may be limited. For example, the experimental structure for the monoclinic and orthorhombic phases of $MPSnBr_3$ [23] have different conformation of the MP molecule, which is likely to originate from the experimental challenges of resolving light hydrogen atoms. Subjecting the MP in the experimental structure to relaxation in computations allows one to overcome this issue and, in principle, should improve accuracy. A somewhat similar approach has been previously applied to MA molecule in $MAPbI_3$ [14] to study the effect of the structure on the Rashba parameter. Therefore, we chose MP relaxation only as our second computational strategy and label associated structures as MP relaxed.

Our third computations strategy is computing ensemble-average structure using AIMD as already described. The associated structures are labeled as Ensemble average. The fourth computational strategy is full structural relaxation of the experimental structures, which usually preserves the space group. We label structures obtained through such an approach as Fully relaxed. As argued in Ref. [14] for the case of $MAPbI_3$ probing the potential energy surface at zero temperature, as is done in DFT structural relaxations, is inadequate to compute the structures of high-temperature phases. One additional concern is that such relaxations neglect the effect of thermal expansion. This concern, however, could be alleviated by keeping lattice vectors in computations equal to those available from experimental data while allowing full ionic relaxation. This approach has been widely applied [7,8,40]. We include this strategy as our fifth approach and label associated structures as Ionically relaxed. To quantify the structural differences between the atomic positions of the phase obtained using different computational strategies, we use the tool of the Bilbao Crystallographic Server, i.e., the COMPSTRU [41,42]. The program COMPSTRU compares two structure descriptions of the same compound characterizing the similarity of the two structure models by an appropriate quantitative descriptor, such as Δ [43]. This descriptor includes the difference in the atomic position and ratios of lattice parameters of two structures, and it is zero for identical structures. We typically
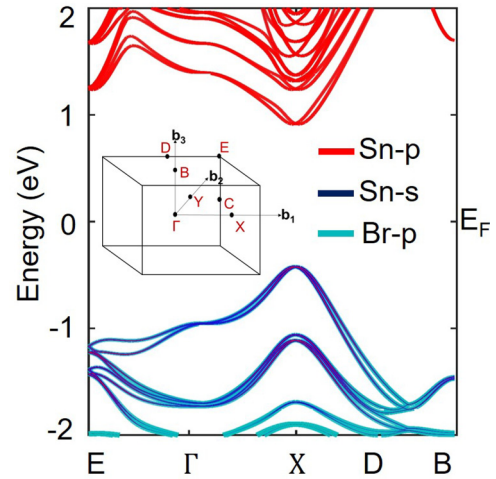

FIG. 4. Orbital resolved SOC band structure of monoclinic $MPSnBr_3$ along high symmetry path.

compute the structural descriptor between a given structure and its fully relaxed version to find out which structures are closest to the reference point. In this way, we can compare the degree of similarity of the different structural models, which are the results of the different computational schemes, with respect to a common reference point.

III. RESULTS AND DISCUSSION

A. Ground-state properties

We begin our investigation with the ground-state properties of $MPSnBr_3$. To obtain the ground state, we subject the experimentally reported 293 K monoclinic phase to full structural optimization as described in Sec. II. To make sure that the fully relaxed structure is not associated with a saddle point in the energy landscape, we subjected it to 2.5 ps AIMD simulations at 100 K. The structure harvested at the end of the simulations was fully optimized and found to be very similar to the one obtained from full structural relaxation only, which confirms that our fully relaxed structure does not correspond to a saddle point in the energy landscape. The fully relaxed structure has Pc space group. Its structural parameters are reported and compared with experimental values in Table I.

We find that the computational lattice parameters and volumes are within 2% and 4% of experimental values, respectively, while $\Delta = 0.05$. The ground-state structure is available from [44]. Table I also reports band gaps and polarization for the ground state and provides a comparison with the data from the literature. Our PBE band gap underestimates the experimental one as expected. Our polarization of 3.0 $\mu C/cm^2$ is in line with the values for other HOIP [2] but lower than 4.5 $\mu C/cm^2$ reported from DFT-PBE simulations [23], possibly due to the difference in the dispersion corrections.

Since the ground state is noncentrosymmetric, it has the potential to exhibit Rashba-Dresselhaus effects due to SOC [45]. To investigate that, we computed SOC-resolved band structure and report it in Fig. 4. For halide perovskites ABX_3, the electronic structure around the Fermi level is governed

TABLE I. Lattice parameters, volumes, band gaps, and electric polarizations of the Pc phase at 0 K computed in this work and computed at 0 K in Ref. [23].

	This work	Ref. [23]
Lattice parameters (Å)	5.98, 11.72, 11.79	6.05, 11.90, 11.98
Monoclinic angle	91.03°	91.71°
Volume Å^3	828.37	863.17
Band gap (eV)	1.02	2.62
Polarization vector and magnitude ($\mu C/cm^2$)	(1.4, 0.0, 2.7) 3.0	4.5 [0 K DFT-PBE]

by states emerging from the $B - s$, $p - X - p$ hybridization. Therefore, we observe the conduction band (CB) is dominated by Sn-p orbitals and the valence band (VB) is mainly of Br-p character along with the Sn-s orbital contribution. SOC lifts band degeneracy near the conduction band minimum (CBM) and valence band maximum (VBM), which is highly desirable for applications [46,47]. For example, along the Γ-X-Γ direction of the Brillouin zone, computations predict splitting of 3.3 meV in the CB and 0.8 meV in VB in the neighborhood of X point, where CBM and VBM occur. Our values are compared with some of the values from the literature for both HOIP and some inorganic materials in Table II. We find that spin splitting in MPSnBr$_3$ is smaller than the ones reported for MAPbI$_3$ and MAPbBr$_3$, which is expected as heavy Pb is replaced with lighter Sn. The value is also significantly smaller than for GeTe, which we use here as an inorganic structure for comparing the calculated Rashba splittings. In Table II the Rashba parameter ($\alpha_R = \frac{2\Delta E}{k_0}$) is also reported. In this case, for MAPbI$_3$ we included the value from Ref. [14] in Table II, which reveals that α_R in lead-free MPSnBr$_3$ is comparable to the one for MAPbI$_3$.

Next we turn to the investigation of spin textures. The point group for the ground state of MPSnBr$_3$ is Cs (contains a mirror plane), whose effective Hamiltonian is [22]

$$H = \frac{\hbar^2}{2}\left(\frac{k_x^2}{m_x} + \frac{k_y^2}{m_y} + \frac{k_z^2}{m_z}\right) + \alpha k_x \sigma_y$$
$$+ k_y(\beta \sigma_x + \gamma \sigma_z) + k_z \delta \sigma_y, \qquad (1)$$

where k_i is the ith Cartesian component of the k vector in Brillouin zone and m_i are the effective masses along ith

TABLE II. Spin splitting strengths, associated vector, and Rashba coefficients of some HOIP and inorganic compounds.

Compound	Region	Energy (ΔE) (meV)	k_0 (Å^{-1})	α_R (eV Å)	Ref.
MAPbI$_3$	CB	136.0	0.080	3.50	[8]
MAPbI$_3$				0.1–0.4 ± 0.2	[14]
MAPbBr$_3$	VB	160.0	0.043	7.40	[9]
FASnI$_3$	CB	9.4	0.016	1.17	[7]
PEPbI$_4$	CB	40.0 ± 5	0.051	~1.60	[10]
(AMP)PbI$_4$	VB	16.0	0.013	2.39	[40]
GeTe	VB	227.0	0.090	4.80	[19]
Bi$_2$WO$_6$	CB	99.4	0.155	1.28	[48]
BiAlO$_3$	VB	7.3	0.039	0.39	[49]
MPSnBr$_3$ (Pc)	CB	3.3	0.011	0.62	This work

Cartesian direction, σ_i are the Pauli spin matrices, while α, β, γ, and δ are the spin-momentum coupling parameters. This Hamiltonian can be diagonalized analytically for different planes in the reciprocal space and used to compute expectation values for spin $\langle \boldsymbol{\sigma} \rangle_\pm$ in the given plane. Here $\pm$ labels the two eigenstates of the Hamiltonian. The dependencies $\langle \boldsymbol{\sigma}_k \rangle$ give origin to spin textures. For Eq. (1) spin textures are expected in (k_x, k_y) and (k_y, k_z) planes, which are perpendicular to the mirror plane (k_z, k_x). Figure 5 presents spin textures in these planes in the vicinity of the CBM and VBM computed from DFT and reveals their well defined structure. Interestingly, we find that the type of spin texture is different between VB and CB, the feature that has been previously reported for inorganic orthorhombic HfO$_2$ [50]. In the (k_x, k_y) we find Rashba type spin textures in the VB and persistent type of spin textures in the CB. Similarly in the (k_y, k_z) plane the VB exhibits the Rashba type spin texture, whereas in CB, near to the center $(k_y = k_z = 0)$, the spin texture appears to be Rashba type and away from center it becomes persistent in nature.

To gain further insight into the origin of these spin textures we turn to the effective Hamiltonian of Eq. (1) and compute spin-momentum locking couplings α, β, γ, and δ. It should be noted that the Hamiltonian of Eq. (1) is written for the Γ point of the Brillouin zone, while in our case VBM and CBM occur in the X point. However, the little group in the X point is the same so we can use the same Hamiltonian. To obtain the parameters we translate the spin-resolved DFT band structure by the reciprocal vector $(1/2,0,0)$ and fit it to eigenvalues of the Hamiltonian of Eq. (1). We note that the band structure alone is not sufficient to decouple β and γ, which necessitates inclusion of $\langle \boldsymbol{\sigma} \rangle_\pm$ into fitting. It can be shown that in the (k_x, k_y) plane $\langle \sigma_x \rangle_\pm = A_\pm \cos \phi$ and $\langle \sigma_y \rangle_\pm = A_\pm \sin \phi$, where $A_\pm$ and ϕ are the amplitude and phase, respectively. These lead to the additional relationship $\frac{\langle \sigma_y \rangle_\pm}{\langle \sigma_x \rangle_\pm} = \frac{\alpha k_x}{\beta k_y}$ that allows one to decouple β and γ by including data from spin textures into the fitting. Technically, we obtain α from fitting band structure along X'-Γ-X' direction, γ from fitting along Y-Γ'-Y direction, and δ from fitting along Z-Γ'-Z direction. Here prime indicates coordinates of the Brillouin zone point after the shift by $(\frac{1}{2}, 0, 0)$. Then we obtain β from spin textures in the (k_x, k_y) plane as follows: $\beta = \alpha \frac{k_x}{k_y} \frac{\langle \sigma_x \rangle_\pm}{\langle \sigma_y \rangle_\pm}$. The signs of all coefficients are confirmed by comparing spin texture patterns computed from the effective Hamiltonian with the ones obtained from DFT for (k_x, k_y) and (k_y, k_z) planes. Table III reports the couplings, which we obtained from such simultaneous fitting of the DFT band structures and spin textures. It should be noted that the set of coupling reproduces DFT spin textures presented in Fig. 5. The hopping parameters
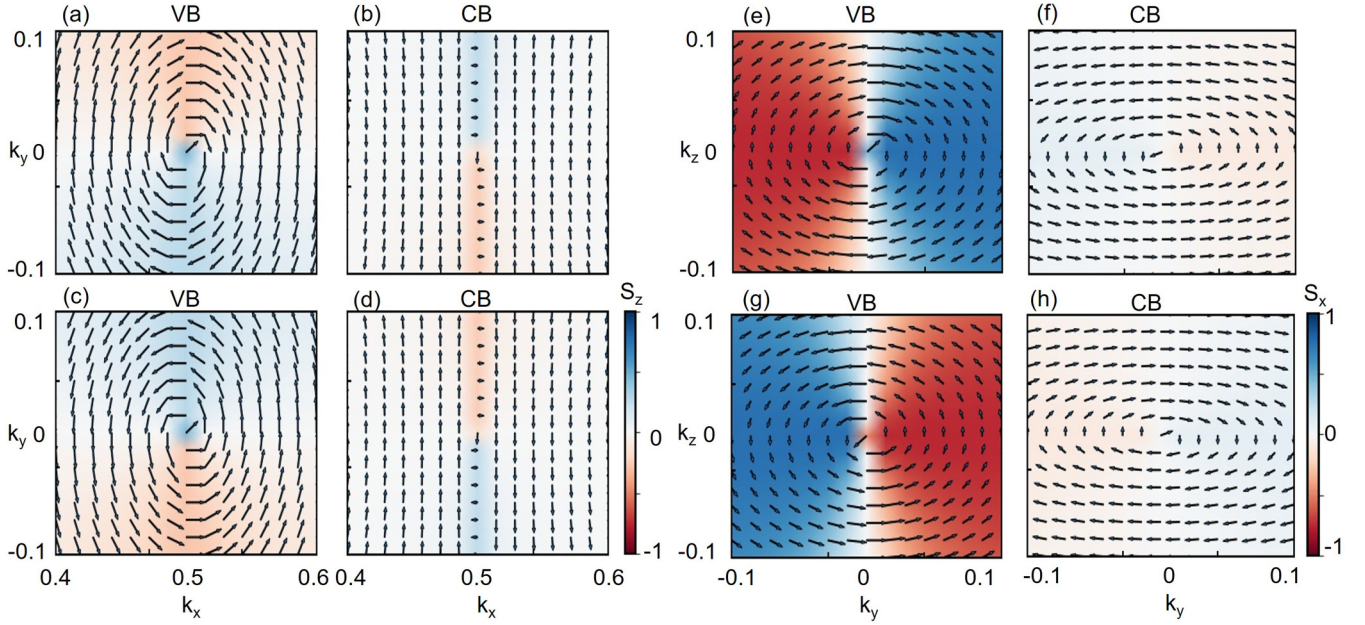
FIG. 5. MPSnBr$_3$ ground-state spin textures for topmost VB [(a) and (e)] and lowermost CB [(b) and (f)] in k_x-k_y and k_y-k_z planes, respectively. Panels (c),(d) and (g),(h) display the same but for the ground state with the reversed polarization direction.

($t_i = \frac{\hbar^2}{2m_i}$ [$i = x, y, z$]) quantify the band curvature along the Cartesian directions and reveal that with the exception of CB along k_y direction both CB and VB are highly dispersive.

In both VB and CB we find the coupling between spin and momentum is stronger in the (k_x, k_y) plane in comparison with (k_y, k_z) as evident from the values of α, β, γ, and δ. This originates from the fact that the polarization component along the direction perpendicular to the (k_x, k_y) plane is larger than the one perpendicular to the (k_y, k_z) plane. Furthermore, we find that the relative strength of the couplings is very different for CB and VB, which explains why we observe different types of spin textures in those bands [15].

The promise of materials that exhibit Rashba effects for potential applications in spintronics is the possibility to control spin textures by the application of electric field [15,19,20,51,52]. Since MPSnBr$_3$ exhibits both Rashba effects and spontaneous polarization it is essential to establish whether they cofunction, which is highly desirable property [15,18,21,53]. To explore this possibility, we inverted the ground-state structure by applying an inversion operation as proposed in Ref. [29] and computed its spin textures. As expected, the polarization for the inverted structure is reversed with respect to the original one. Figure 5 demonstrates that the reversal of polarization is associated with the reversal of

spin textures, which establishes the possibility of their control through the application of the electric field. This allows us to conclude that MPSnBr$_3$ exhibits cofunctionality between Rashba effects and ferroelectricity.

Thus our calculations predict (1) the existence of near band edge spin splitting in both VB and CB of MPSnBr$_3$ ground state, with the values of 0.8 and 3.3 meV, respectively, (2) spin textures of different types in the CB and VB, which appear in two orthogonal planes of the Brillouin zone, and (3) coupling between the spin textures and electric polarizations, which establishes the cofunctionality between ferroelectric order parameter and Rashba effects.

B. Temperature dependence

In this section we aim to extend the structure descriptions to finite temperatures. To achieve that we focus on MPSnBr$_3$ monoclinic and orthorhombic phases at 293 and 333 K, respectively, as these are the temperatures for which experimental data are available. Our main computational strategy is AIMD as described in Sec. II. All properties at finite temperatures (polarizations, band structures, band gaps, and spin textures) are computed for the ensemble-average structures. It should be noted that the ensemble-average structure does not preserve the symmetry of the phase which was used for the simulation initialization. Consequently, both ensemble-average structures have $P1$ symmetry. Nevertheless, the ensemble-average and experimental structures are close to each other, with $\Delta = 0.015$ and 0.019 (without hydrogen atoms) for the monoclinic and orthorhombic phases, respectively. We will use the terms monocliniclike and orthorhombiclike to refer to these ensemble-average structures. We computed SOC resolved band structures, band gaps, and polarizations for both phases and include some of the data in Table V. These data can be combined with our predic-

TABLE III. Hopping parameters $t_i = \frac{\hbar^2}{2m_i}$ [$i = x, y, z$] and spin-momentum coupling parameters (α-δ) in eV Å^{-2} and eV Å, respectively, computed in the ground state of MPSnBr$_3$.

Compound	t_x	t_y	t_z	α	β	γ	δ
VB	-15.42	-18.39	-19.48	-0.22	0.15	-0.05	0.08
CB	14.42	6.39	11.80	0.46	0.00	-0.06	-0.11

TABLE IV. Hopping parameters $t_i = \frac{\hbar^2}{2m_i}$ [$i = x, y$] and spin-momentum coupling parameters (α and β) in eV Å^{-2} and eV Å, respectively, computed for the ensemble-average structures at 333 K.

Compound	t_x	t_y	α	β
CB	10.42	11.27	0.11	0.25
VB	−17.42	−19.42	0.05	−0.11

tions for the ground state to assess temperature evolution of these properties. For polarization we predict 3.06, 2.67, and 0.15 μC/cm^2 at temperatures 0, 293, and 333 K, respectively. The polarization decreases in magnitude as temperature increases and reduces significantly in the orthorhombiclike phase. At the same temperatures the band gaps are 1.02, 1.30, and 1.32 eV, respectively. There is significant increase in the band gap in the monocliniclike phase as the temperature is increased from 0 to 293 K. This is due to the fact that at 0 K, the volume of the unit cell is smaller than that at 293 K (see Table V). Analysis of the effect of pressure on MPSnBr$_3$ monoclinic and orthorhombic unit cell infers that the band gap indeed decreases with pressure. Volume compression due to pressure increases the covalent interactions within the octahedra cage, which increase the width of the bands. The band gaps in the orthorhombiclike and monocliniclike phases are comparable.

Let us now focus on Rashba effects at finite temperatures. For the ensemble-average structure at 293 K the band structure is similar to the one reported in Fig. 4. The band structure for the ensemble-average structure at 333 K is given in Fig. 6 and reveals direct band gap at Γ point. All band structures possess spin splittings. We find the following temperature evolution of spin splitting in the CB: 3.3, 5.1, and 2.9 meV for the temperatures 0, 293, and 333 K, respectively. In the VB the respective values are 0.8, 0.8, and 0.1 meV. Overall we find spin splitting to be smaller in the orthorhombiclike phase. The Rashba parameter in the CB is 0.62, 0.64, and

0.41 eV Å at 0, 293, and 333 K, respectively. In the VB it is 0.30, 0.30, and 0.06 eV Å at the same temperatures. Spin textures obtained for the ensemble-average structure at 293 K are very similar to the ground-state ones reported in Fig. 6. For the orthorhombiclike phase, the VBM and CBM occur at Γ. As our ensemble-average structure is close to the orthorhombic $Pna2_1$ phase from which it was derived, we will use the Hamiltonian for the C_{2v} point group symmetry [15]:

$$H = \frac{\hbar^2}{2}\left(\frac{k_x^2}{m_x} + \frac{k_y^2}{m_y}\right) + \alpha k_x \sigma_y + \beta k_y \sigma_x. \quad (2)$$

The spin textures are expected in the (k_x, k_y) plane, although we note again that ensemble averaging does not preserve the symmetry of the experimental phase. Figure 6 shows spin textures for the ensemble-average structure in the (k_x, k_y) plane. The spin textures are primarily persistent in the VB and CB, respectively, with Rashba and Dresselhaus components. To explain that we compute Rashba and Dresselhaus parameters, as $\lambda_R = (\alpha - \beta)/2$ and $\lambda_D = (\alpha + \beta)/2$ [15], where we use values for α and β reported in Table IV. For the CB we obtain $\lambda_R = -0.07$ and $\lambda_D = 0.18$ eV Å^{-2}, which confirms that the spin texture has Dresselhaus nature along with the persistent type. Similarly, for the VB we find $\lambda_R = 0.08$ and $\lambda_D = -0.03$ eV Å^{-2}, which infers the Rashba type spin texture along with the persistent type. Furthermore, we find that the spin-momentum coupling parameters are smaller in the orthorhombic phase as compared to monoclinic phase (compare Tables III and IV). We computed spin textures for 293 and 333 K structures with reversed direction of polarization and found them to be reversed; that is, the coupling between spin textures and polarization direction persists at finite temperatures.

We note that the temperature evolution of polarization and spin splitting are not correlated in this case. This is likely due to the fact that spin splitting occurs in the bands that originate from Sn-p and s orbitals of the framework, while the polarization originates primarily from the dipole moment of the MP molecule. As the framework and molecules may evolve in temperature differently, this could give rise to differences in the temperature evolution of spin splitting and polarization.

Thus extending our investigation to finite temperatures reveals (1) that spin splitting occurs at finite temperatures and exhibits comparable values in a given band for the temperatures studied, (2) the presence of spin textures at all investigated temperatures and in both monocliniclike and orthorhombiclike phases, and (3) that spin textures are coupled to the direction of polarization for all considered temperatures, so the cofunctionality between ferroelectricity and Rashba effects is preserved in a wide temperature range.

C. Dependence of finite temperature predictions on computational strategy for structural optimization

In this section we aim to find out how properties discussed in the previous section are affected by the choice of computational strategy. As described in Sec. II, we have considered five computational strategies to extend predictions to finite temperature. Table V summarizes our data obtained using
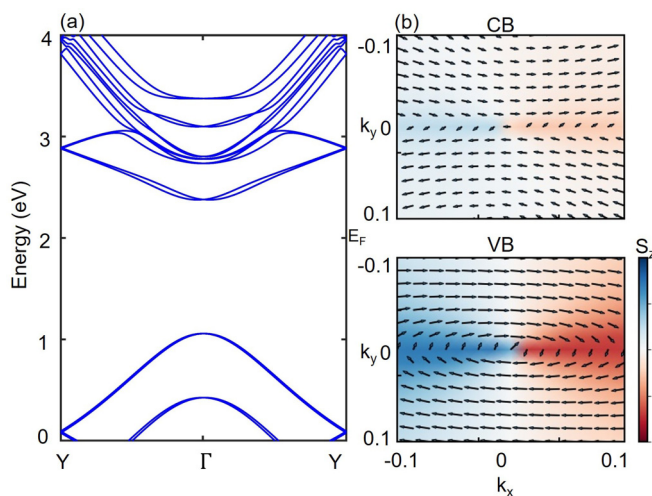

FIG. 6. (a) Band structure of ensemble-average structure at 333 K. (b) Spin texture of lowermost conduction band and uppermost valence band for the same structure in k_x-k_y plane.

TABLE V. Energy, internal stress, band gap, electric polarization, and structural descriptor of structures computed using five computational strategies. Energy is reported with respect to ground-state value. Experimental and ensemble-average structures correspond to 293 and 333 K for monoclinic and orthorhombic phases, respectively, while the rest of the structures correspond to 0 K.

Components		Monoclinic (*Pc*)	Orthorhombic (*Pna*2₁)
Lattice parameters (Å)	Fully relaxed	5.98, 11.72, 11.79	11.84, 9.06, 7.90
	Expt.	6.05, 11.90, 11.98	12.02, 9.08, 8.08
Monoclinic angle	Fully relaxed	91.03°	
	Expt.	91.71°	
Volume (Å³)	Fully relaxed	828.37	848.84
	Expt.	863.17	882.81
	Expt.	1.45	1.5
	Ensemble average	0.02	0.05
Energy (eV/f.u.)	MP relaxed	0.04	0.09
	Ionically relaxed	0.01	0.05
	Fully relaxed	0.00	0.04
	Expt.	6.45	6.5
	Ensemble average	−0.45	−0.25
Stress (GPa)	MP relaxed	0.13	0.12
	Ionically relaxed	−0.40	−0.40
	Fully relaxed	0.00	0.00
	Expt.	1.34	1.32
	Ensemble average	1.30	1.32
Band gap (eV)	MP relaxed	1.44	1.34
	Ionically relaxed	1.24	1.31
	Fully relaxed	1.02	1.13
	Expt.	(0.11, 0.00, 2.86) 2.86	(0.00, 0.00, 0.00) 0.00
Polarization vector	Ensemble average	(1.11, 0.02, 2.43) 2.67	(0.15, 0.04, 0.03) 0.15
and	MP relaxed	(0.35, 0.00, 4.03) 4.03	(0.00, 0.00, 0.30) 0.30
magnitude (μC/cm²)	Ionically relaxed	(1.13, 0.00, 2.85) 3.06	(0.00, 0.00, 0.79) 0.79
	Fully relaxed	(1.42, 0.00, 2.73) 3.06	(0.00, 0.00, 1.50) 1.50
	Expt.	0.05	0.08
	Ensemble average	0.02	0.06
Structural	MP relaxed	0.03	0.03
descriptor (Δ)	Ionically relaxed	0.01	0.01
	Fully relaxed	0.00	0.00

these strategies. For those structures, which incorporate lattice vector relaxation, we list the computed lattice parameters and volumes and compare them with experimental data. Our lattice parameters are within 2% of experimental values, while volumes are within 4%.

Energetically, full structural relaxation produces the lowest energy structure for a given phase as it corresponds to zero kelvin. From inspections of energies for different structures reported in Table V we find that both experimental phases are significantly higher in energy than the structures produced in the simulations, about 1.4 eV/f.u. The significant energy difference between MP relaxed and experimental structures suggests that the MP molecules' relaxation is responsible for the significant energy difference between experimental and computational structures. As already noted in Sec. II, resolving hydrogen atoms experimentally could be challenging and prone to inaccuracies. Therefore, we believe that computational relaxation allows one to correct for that, which explains significant energy lowering that occurs upon MP relaxation. All structures obtained in computations are energetically very

close to each other, within 0.04 eV/f.u. Inspection of the stresses reveals large values associated with experimental structures, while the stresses are low for all other relaxation techniques. We also report the structural descriptor between a given structure and its fully relaxed version in Table V. For the monoclinic phase, as expected, the more degrees of freedom that are allowed to relax, the closer the structure is to the fully relaxed one. The data for the orthorhombic phase is surprising, though, as we find that the ensemble-average structure is the furthermost away from the fully relaxed one among the computational structures. This finding indicates that probing the 0 K energy surface in this material may not provide an adequate description for the finite temperature structure.

We find the band gap to be dependent on the choice of computational strategy. The band gap of ensemble-average structures agrees very well with those of experimental ones, while the band gap for fully relaxed structures is 24% and 14% lower than for the experimental one. This originates from the differences in the ionic positions within SnBr₃ octahedra. For the polarizations, we find closest agreement between

TABLE VI. Spin-splitting strength, associated k points, and Rashba coefficients along Γ-X-Γ and Y-Γ-Y for monoclinic and orthorhombic structures, respectively, for VB and CB.

Type	Region	Monoclinic			Orthorhombic		
		Energy (meV)	k_0 (Å^{-1})	α_R (eV Å)	Energy (meV)	k_0 (Å^{-1})	α_R (eV Å)
Expt.	VB	1.90	0.005	0.72	0.0	0.0	0.00
	CB	13.6	0.026	1.03	0.3	0.004	0.17
Ensemble average	VB	0.8	0.005	0.30	0.1	0.003	0.06
	CB	5.1	0.016	0.64	2.9	0.014	0.41
MP relaxed	VB	1.1	0.005	0.42	0.0	0.000	0.00
	CB	12.9	0.026	0.98	0.3	0.004	0.17
Ionically relaxed	VB	0.8	0.005	0.30	0.8	0.007	0.23
	CB	3.2	0.010	0.61	14.6	0.031	0.93
Fully relaxed	VB	0.8	0.005	0.30	1.5	0.007	0.42
	CB	3.3	0.011	0.62	22.5	0.038	1.17

experimental and ensemble-average structures. For the orthorhombic phase, the fully relaxed structure possesses the largest polarization, which is 10 times enhanced with respect to the ensemble-average one.

Next, we compute SOC resolved band structures, Rashba coefficients, and spin textures for each of the structures reported in Table V and summarize spin-splitting, k_0, and Rashba coefficient data in Table VI. The data suggest that all the reported parameters depend on the choice of the computational approach. For example, in the monoclinic phase the spin splitting in the CB is 13.6 meV for the experimental structure, while only 3.3 meV for the fully relaxed structure. For the orthorhombic phase, it is 0.3 and 22.5 meV in the CB for the experimental and fully relaxed structure, respectively. A comparison of the actual values suggests that the most significant change in the values occurs once we allow SnBr$_6$ octahedra relaxation, which is consistent with the fact that the VB is dominated by Sn-s and Br-p orbitals. On the other hand, spin splitting is almost insensitive to the relaxation of the MP molecules. These trends agree with the findings for MAPbI$_3$ [14].

It should also be realized that the spin splitting in MPSnBr$_3$ is relatively small, which could amplify its dependence on the choice of computational strategy. For further insight, we turn to GeTe and investigate sensitivity of spin splitting to structure in this well studied material. We found that spin splitting in the VB predicted for the experimental structure of Ref. [19] is 125 meV. Allowing ionic relaxation while keeping the lattice vectors as in experiment results in the value of 233 meV, which is in good agreement with 227 meV predicted computationally in Ref. [19], using a similar relaxation strategy. Allowing full structural relaxation leads to significant enhancement of the value up to 301 meV. These findings support that spin splitting is highly sensitive to the structural details, which in turn are dependent on the choice of computational methodology.

Thus we found that band structures, Rashba effects, and polarization in MPSnBr$_3$ are sensitive to the choice of computational approach for structural optimization. Ensemble-average structures produced with the help of AIMD exhibit properties that match most closely the ones computed for ex-

perimental structures. Using full structural relaxation to obtain a high-temperature orthorhombic phase leads to the values' polarization, Rashba effects, and band gaps that are further away from those obtained for the experimental structure. Polarization and Rashba effects are strongly enhanced in this case.

IV. CONCLUSIONS

In summary, we have applied DFT computations to investigate ferroelectricity, Rashba effects, and their cofunctionality in lead-free HOIP MPSnBr$_3$. We found the ground state of being of monoclinic Pc space group with spontaneous polarization of 3.01 μC/cm^2. It exhibits spin splitting of 3.3 and 0.8 meV near the edges of CB and VB, respectively. While the presence of spin splitting near band edges is very attractive from an application point of view, the small value may allow for functionality only at low temperatures. The spin-momentum coupling results in the presence of spin textures in the two orthogonal planes near the X point of the Brillouin zone. One interesting feature is that spin textures in the VB differ from those of CB. The spin textures are coupled to the direction of polarization; the material exhibits ferroelectricity Rashba effect simultaneousness, which is a highly desirable feature. Through the use of AIMD we extended our predictions to finite temperatures. The properties of the monocliniclike phase at 293 K are very similar to the ground state with minor quantitative differences. In the orthorhombiclike phase at 333 K we find that the polarization value decreased to 0.15 μC/cm^2. The spin splitting decreases to 2.9 and 0.1 meV in the CB and VB, respectively. The conjunction between ferroelectricity and Rashba effects is preserved in the orthorhombiclike phase. The Rashba coefficient for MPSnBr$_3$ is in the range of 0.06–0.64 eV Å, which is lower than for the inorganic compounds (0.4–4.8 eV Å), but comparable to lead-based MAPbI$_3$ (see Table II). Therefore, MPSnBr$_3$ could be a promising material for low-temperature applications in spintronics or quantum computing.

We have assessed the role of computational methodology in predicting the aforementioned properties by considering five strategies, many of which are widely used. We found that

structures produced with the help of AIMD result in properties that match most closely those obtained for experimental structures. On the other hand, using full relaxation to obtain high-temperature phases results in properties that are significantly different from the ones predicted for experimental structures and often enhanced. Overall, we found predictions to be sensitive to the choice of computational methodology. Interestingly, this remains the case even for the famous inorganic Rashba material GeTe.

Our study advances in understanding of the recently synthesized lead-free HOIP MPSnBr$_3$ [23], reveals its potential for applications in spintronics, and highlights methodological challenges for finite-temperature predictions.

[1] W. Li, Z. Wang, F. Deschler, S. Gao, R. H. Friend, and A. K. Cheetham, Nat. Rev. Mater. **2**, 16099 (2017).

[2] W. Li, A. Stroppa, S. Gao, and Z. M. Wang, *Hybrid organic-inorganic perovskites* (John Wiley & Sons, New Jersey, 2020).

[3] T. M. Brenner, D. A. Egger, L. Kronik, G. Hodes, and D. Cahen, Nat. Rev. Mater. **1**, 15007 (2016).

[4] S. Shahrokhi, W. Gao, Y. Wang, P. R. Anandan, M. Z. Rahaman, S. Singh, D. Wang, C. Cazorla, G. Yuan, J.-M. Liu, and T. Wu, Small Methods **4**, 2000149 (2020).

[5] P. S. Whitfield, N. Herron, W. E. Guise, K. Page, Y. Q. Cheng, I. Milas, and M. K. Crawford, Sci. Rep. **6**, 35685 (2016).

[6] M. Kepenekian, R. Robles, C. Katan, D. Sapori, L. Pedesseau, and J. Even, ACS Nano **9**, 11557 (2015).

[7] A. Stroppa, D. Di Sante, P. Barone, M. Bokdam, G. Kresse, C. Franchini, M.-H. Whangbo, and S. Picozzi, Nat. Commun. **5**, 5900 (2014).

[8] S. Hu, H. Gao, Y. Qi, Y. Tao, Y. Li, J. R. Reimers, M. Bokdam, C. Franchini, D. Di Sante, A. Stroppa, and W. Ren, J. Phys. Chem. C **121**, 23045 (2017).

[9] D. Niesner, M. Wilhelm, I. Levchuk, A. Osvet, S. Shrestha, M. Batentschuk, C. Brabec, and T. Fauster, Phys. Rev. Lett. **117**, 126401 (2016).

[10] Y. Zhai, S. Baniya, C. Zhang, J. Li, P. Haney, C. X. Sheng, E. Ehrenfreund, and Z. V. Vardeny, Sci. Adv. **3**, e1700704 (2017).

[11] E. I. Rashba, J. Supercond. **15**, 13 (2002).

[12] G. Dresselhaus, Phys. Rev. **100**, 580 (1955).

[13] M. Kim, J. Im, A. J. Freeman, J. Ihm, and H. Jin, Proc. Natl. Acad. Sci. USA **111**, 6900 (2014).

[14] K. Frohna, T. Deshpande, J. Harter, W. Peng, B. A. Barker, J. B. Neaton, S. G. Louie, O. M. Bakr, D. Hsieh, and M. Bernardi, Nat. Commun. **9**, 1829 (2018).

[15] L. L. Tao and E. Y. Tsymbal, J. Phys. D **54**, 113001 (2021).

[16] J. Schliemann, Rev. Mod. Phys. **89**, 011001 (2017).

[17] M. Kohda and G. Salis, Semicond. Sci. Technol. **32**, 073002 (2017).

[18] C. M. Acosta, A. Fazzio, G. M. Dalpian, and A. Zunger, Phys. Rev. B **102**, 144106 (2020).

[19] D. Di Sante, P. Barone, R. Bertacco, and S. Picozzi, Adv. Mater. **25**, 509 (2013).

[20] H. Lee, J. Im, and H. Jin, Appl. Phys. Lett. **116**, 022411 (2020).

[21] F. Lou, T. Gu, J. Ji, J. Feng, H. Xiang, and A. Stroppa, npj Comput. Mater. **6**, 114 (2020).

[22] R. Kashikar, P. S. Ghosh, S. Lisenkov, B. R. K. Nanda, and I. Ponomareva, Phys. Rev. B **104**, 235132 (2021).

[23] H.-Y. Zhang, X.-G. Chen, Z.-X. Zhang, X.-J. Song, T. Zhang, Q. Pan, Y. Zhang, and R.-G. Xiong, Adv. Mater. **32**, 2005213 (2020).

[24] K. Aizu, Phys. Rev. B **2**, 754 (1970).

[25] P. E. Blöchl, Phys. Rev. B **50**, 17953 (1994).

[26] G. Kresse and J. Furthmüller, Phys. Rev. B **54**, 11169 (1996).

[27] S. Grimme, J. Comput. Chem. **27**, 1787 (2006).

[28] R. D. King-Smith and D. Vanderbilt, Phys. Rev. B **47**, 1651 (1993).

[29] M. Kingsland, P. S. Ghosh, S. Lisenkov, and I. Ponomareva, J. Phys. Chem. C **125**, 8794 (2021).

[30] H. T. Stokes, B. J. Campbell, and D. M. Hatch, Isotropy, https://stokes.byu.edu/iso/isodistort.php.

[31] H. T. Stokes, D. M. Hatch, B. J. Campbell, and D. E. Tanner, J. Appl. Crystallogr. **39**, 607 (2006).

[32] P. S. Ghosh, D. DeTellem, J. Ren, S. Witanachchi, S. Ma, S. Lisenkov, and I. Ponomareva, Phys. Rev. Lett. **128**, 077601 (2022).

[33] M. Kingsland, Z. G. Fthenakis, and I. Ponomareva, Phys. Rev. B **100**, 024114 (2019).

[34] S. Liu, I. Grinberg, and A. M. Rappe, Nature (London) **534**, 360 (2016).

[35] B. Monserrat and D. Vanderbilt, Phys. Rev. Mater. **1**, 054201 (2017).

[36] B. Monserrat and D. Vanderbilt, Phys. Rev. Lett. **117**, 226801 (2016).

[37] V. Brousseau-Couture, G. Antonius, and M. Côté, Phys. Rev. Res. **2**, 023185 (2020).

[38] T. Etienne, E. Mosconi, and F. De Angelis, J. Phys. Chem. Lett. **7**, 1638 (2016).

[39] M. L. Agiorgousis, Y.-Y. Sun, H. Zeng, and S. Zhang, J. Am. Chem. Soc. **136**, 14570 (2014).

[40] F. Wang, H. Gao, C. de Graaf, J. M. Poblet, B. J. Campbell, and A. Stroppa, npj Comput. Mater. **6**, 183 (2020).

[41] M. Aroyo, J. Perez-Mato, D. Orobengoa, E. Tasci, G. De La Flor, and A. Kirov, Bulg. Chem. Commun. **43**, 183 (2011).

[42] G. de la Flor, D. Orobengoa, E. Tasci, J. M. Perez-Mato, and M. I. Aroyo, J. Appl. Crystallogr. **49**, 653 (2016).

[43] G. Bergerhoff, M. Berndt, K. Brandenburg, and T. Degen, Acta Crystallogr. Sect. B **55**, 147 (1999).

[44] I. Ponomareva, MPSnBr$_3$-Structures, https://github.com/USFmatscilab/MPSnBr3-Structures.

[45] R. Winkler, *Spin-Orbit Coupling Effects in Two-Dimensional Electron and Hole Systems*, Springer Tracts in Modern Physics (Springer, Berlin, 2003).

[46] H. Hatada, M. Nakamura, M. Sotome, Y. Kaneko, N. Ogawa, T. Morimoto, Y. Tokura, and M. Kawasaki, Proc. Natl. Acad. Sci. USA **117**, 20411 (2020).

[47] S.-Y. Wu, IEEE Trans. Electron Devices **21**, 499 (1974).

[48] H. Djani, A. C. Garcia-Castro, W. Y. Tong, P. Barone, E. Bousquet, S. Picozzi, and P. Ghosez, npj Quantum Mater. **4**, 51 (2019).

[49] L. G. D. da Silveira, P. Barone, and S. Picozzi, Phys. Rev. B **93**, 245159 (2016).

[50] L. L. Tao, T. R. Paudel, A. A. Kovalev, and E. Y. Tsymbal, Phys. Rev. B **95**, 245141 (2017).

[51] D. V. Khomitsky, Phys. Rev. B **79**, 205401 (2009).

[52] M. Gupta and B. R. K. Nanda, Phys. Rev. B **105**, 035129 (2022).

[53] S. Picozzi, Front. Phys. **2**, 10 (2014).